NANO LETTERS

Letter

pubs.acs.org/NanoLett

Hybrid Tip-Enhanced Nanospectroscopy and Nanoimaging of Monolayer WSe_2 with Local Strain Control

Kyoung-Duck Park,[†] Omar Khatib,[†] Vasily Kravtsov,[†] Genevieve Clark,[‡] Xiaodong Xu,[‡] and Markus B. Raschke*[,†]

[†]Department of Physics, Department of Chemistry, and JILA, University of Colorado, Boulder, Colorado 80309, United States

[‡]Department of Physics, Department of Materials Science and Engineering, University of Washington, Seattle, Washington 98195, United States

Supporting Information

ABSTRACT: Many classes of two-dimensional (2D) materials have emerged as potential platforms for novel electronic and optical devices. However, their physical properties are strongly influenced by nanoscale heterogeneities in the form of edges, twin boundaries, and nucleation sites. Using combined tip-enhanced Raman scattering and photoluminescence (PL) nanospectroscopy and nanoimaging, we study the associated effects on the excitonic properties in monolayer WSe_2 grown by physical vapor deposition. With ~15 nm spatial resolution, we resolve nanoscale correlations of PL spectral intensity and shifts with crystal edges and internal twin boundaries associated with the expected exciton diffusion length. Through an active atomic force tip interaction we can control the crystal strain on the nanoscale and tune the local bandgap in reversible (up to 24 meV shift) and irreversible (up to 48 meV shift) fashion. This allows us to distinguish the effect of strain from the dominant influence of defects on the PL modification at the different structural heterogeneities. Hybrid nano-optical spectroscopy and imaging with nanomechanical strain control thus enables the systematic study of the coupling of structural and mechanical degrees of freedom to the nanoscale electronic and optical properties in layered 2D materials.

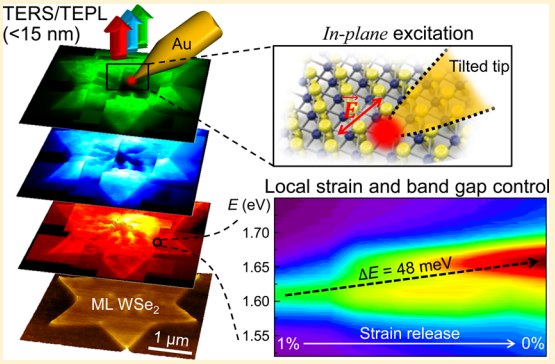

KEYWORDS: *Tip-enhanced photoluminescence (TEPL), tip-enhanced Raman spectroscopy (TERS), transition metal dichalcogenides (TMD), tungsten diselenide (WSe_2), strain, grain boundary*

Layered two-dimensional (2D) transition metal dichalcogenides (TMDs) have emerged as a new platform for studying quantum confined semiconductor physics.[1−5] As the TMD crystals are thinned to the monolayer (ML) limit, new properties emerge including an indirect-to-direct bandgap transition,[6−8] valley-specific circular dichroism,[9−12] or an enhanced nonlinear optical response.[13,14] The direct semiconducting gap, large spin−orbit coupling, and valley-selectivity provide several advantages for the use of TMDs in photodetector and other optoelectronic device applications.

A prevailing theme in TMDs and other layered van der Waals systems is the complex interaction between fundamental excitations inherent to the materials themselves, and extrinsic factors associated with surface morphology and the underlying substrate. In addition, the reduced dimensionality invites strong interference from impurities, defects, and disorder, creating much difficulty in isolating the intrinsic quantum properties of the material.[15] The resulting electronic properties are consequently highly inhomogeneous and sensitive to structural variations near internal and external boundaries.[16,17] To explore these heterogeneities and how they control the optical and electronic properties, a comprehensive multimodal nanoscale imaging and spectroscopy approach is desired.

High-resolution local probes such as scanning tunneling microscopy (STM) and transmission electron microscopy (TEM) uncover the specific nature of structural defects and grain boundaries (GBs) that may lead, for example, to an increase or decrease in the electrical conductivity.[16,18,19] However, despite atomic-scale spatial resolution, these experimental techniques provide limited information on the associated electronic, spin, or optical response. To this end, a series of recent studies applying confocal[16,17,20] and near-field photoluminescence (PL) mapping[21,22] with spatial resolution reaching as high as ~60 nm have addressed the question of the local modification of the optical and electronic properties at GBs. However, both increases and decreases in PL quantum yield have been observed for different crystal geometries and sizes.[16,17,21,22] The range of studies have left a confusing picture regarding the relative role of doping, defects, midgap exciton states, or strain controlling the PL intensity, line shape, and spectral position associated with structural heterogeneities.

Received: January 20, 2016
Revised: February 28, 2016
Published: March 3, 2016

DOI: 10.1021/acs.nanolett.6b00238
Nano Lett. 2016, 16, 2621−2627

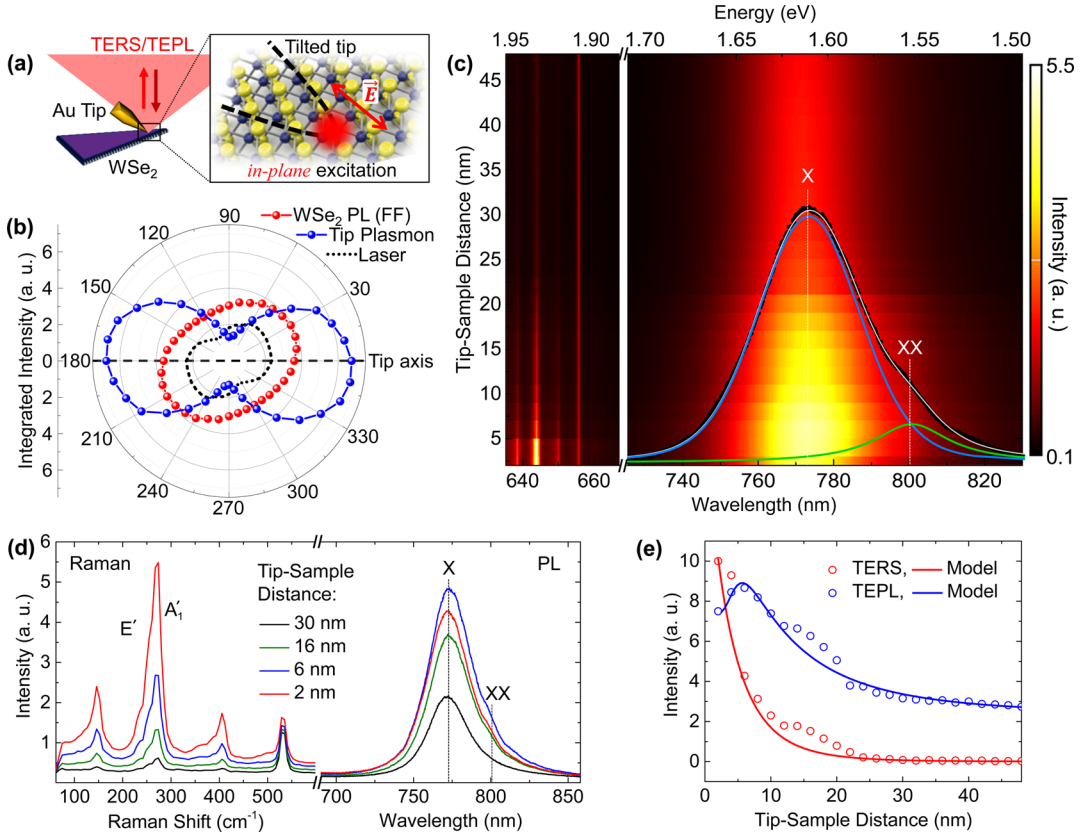

Figure 1. Schematic of multimodal TEPL/TERS (a) with polar plot of the integrated intensity (b) for the tip plasmon (blue line), WSe_2 PL (red line), and excitation laser (black line). (c) Tip−sample distance dependence of TEPL and TERS of monolayer WSe_2. Measured TEPL spectrum (black) at 6 mm distance with Voigt profile fit (gray) decomposed into exciton (blue, X), and possibly biexciton (green, XX) emission. (d) Selected TERS and TEPL spectra for different tip−sample distances. (e) Peak intensity dependence of WSe_2 Raman (273 cm^{-1}) and WSe_2 PL response (772 nm) with respect to the tip−sample distance, derived from (c) with fit to rate equation model as described in Supporting Information.

Here, we present a new hybrid nano-optomechanical tip-enhanced spectroscopy and imaging approach combining nano-Raman (tip-enhanced Raman scattering, TERS), nano-PL (tip-enhanced photoluminescence, TEPL), and atomic force local strain control to investigate the correlation of local structural heterogeneities with nanoscale optical properties with enhanced ∼15 nm spatial resolution. Using a novel tilted tip approach for in-plane near-field polarization control, we study the excited state PL response in twinned WSe_2 ML physical vapor deposition (PVD) grown microcrystals. A combination of PL quenching and selective spectral changes at nanoscale defects is resolved on tens of nanometers length scales. Specifically, local PL quenching and a spectral blueshift are observed at crystal edges and nucleation sites (NS) attributed to energy funneling in the heterogeneous system and nonuniform composite ratio between W and Se, respectively. On the other hand, only PL quenching is observed without change in energy at twin boundaries (TBs) over ∼30 nm length scales correlated with exciton diffusion into nonradiative recombination center. In addition, through controlled tip−sample force interaction we can tune the bandgap reversibly (up to 24 meV) and irreversibly (up to 48 meV) through local nanoscale strain engineering (0−1%). The combined results allow for the separation of the effect of strain from controlling the PL modification at edges, NS, and TBs and suggest defects and stoichiometry as the primary factors modifying the PL at the structural heterogeneities but in distinctly different ways. These results clarify many of the apparent inconsistencies of earlier studies. This shows the potential of combined nano-optical and nanomechanical spectroscopy and imaging with nanometer spatial resolution, few cm^{-1} spectral resolution, and nN force sensitivity as generally applicable to a wide range of systems beyond 2D materials.

Experimental Section. As shown schematically in Figure 1a, the experiment is based on a confocal microscope setup with top illumination of a shear-force atomic force microscope (AFM) tip for combined TERS and TEPL (see Methods and Figure S1a for detail). After passing through a half wave plate for polarization control, a helium−neon laser beam (632.8 nm, < 0.5 mW) is focused onto the WSe_2 sample by an objective lens (100× , NA = 0.8). The electrochemically etched Au-tip with typical apex radius (r ∼ 15 nm) is then positioned in the focal area.[23] With the tip tilted by ∼40° with respect to the surface normal, confocal far-field or TERS and TEPL imaging and spectroscopy can then be performed alternatively by simply retracting or engaging the plasmonic Au-tip with the sample. The resulting localized surface plasmon resonance (LSPR) excitation in the axial direction of the tip with "in-plane" sample projection of the locally enhanced near-field leads to effective excitation of the in-plane Raman and exciton modes as characteristic for layered 2D materials. This is in contrast to conventional surface normal excitation for normal tip orientation (see Figure S1b for details). Figure 1b shows the resulting anisotropy of the tip scattered plasmon response (blue) and far-field WSe_2 PL (red) as a function of excitation polarization (black, slightly asymmetric due to the polarization-

DOI: 10.1021/acs.nanolett.6b00238
Nano Lett. 2016, 16, 2621−2627

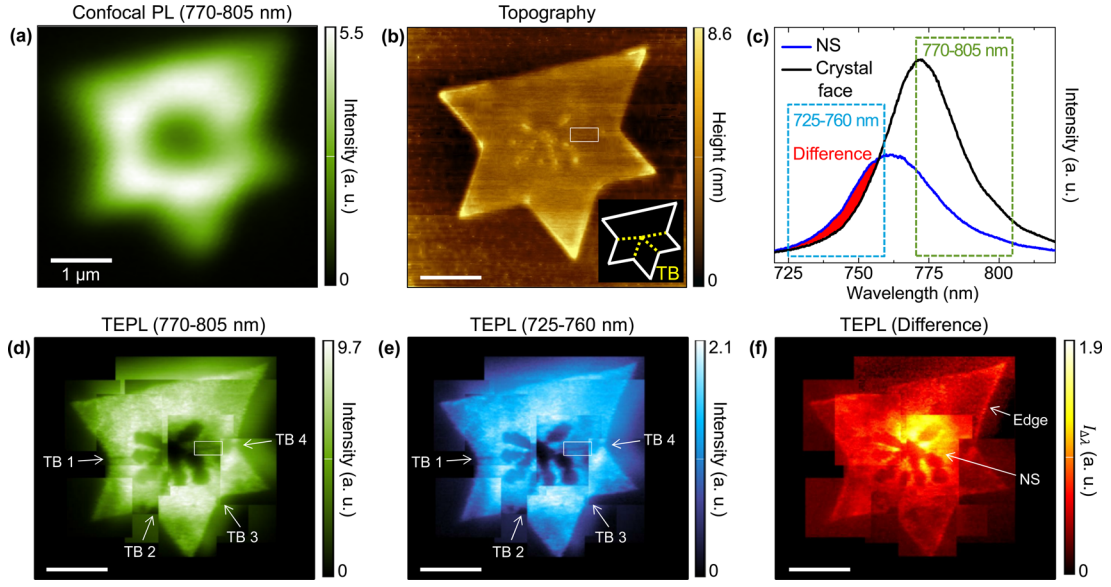

Figure 2. (a) Confocal PL images of a ML WSe_2 crystal for the integrated intensity from 770−805 nm (Blueshifted PL (725−760 nm) and spectral difference PL images are shown in Figure S3a,b). (b) Corresponding topography with inset illustrating the crystal and TBs. (c) TEPL spectra of the ML WSe_2 for nucleation site (NS) and grain face regions. TEPL images for the integrated intensity of 770−805 nm (d) and 725−760 nm (e) spectral regions, and spectral difference TEPL image (f).

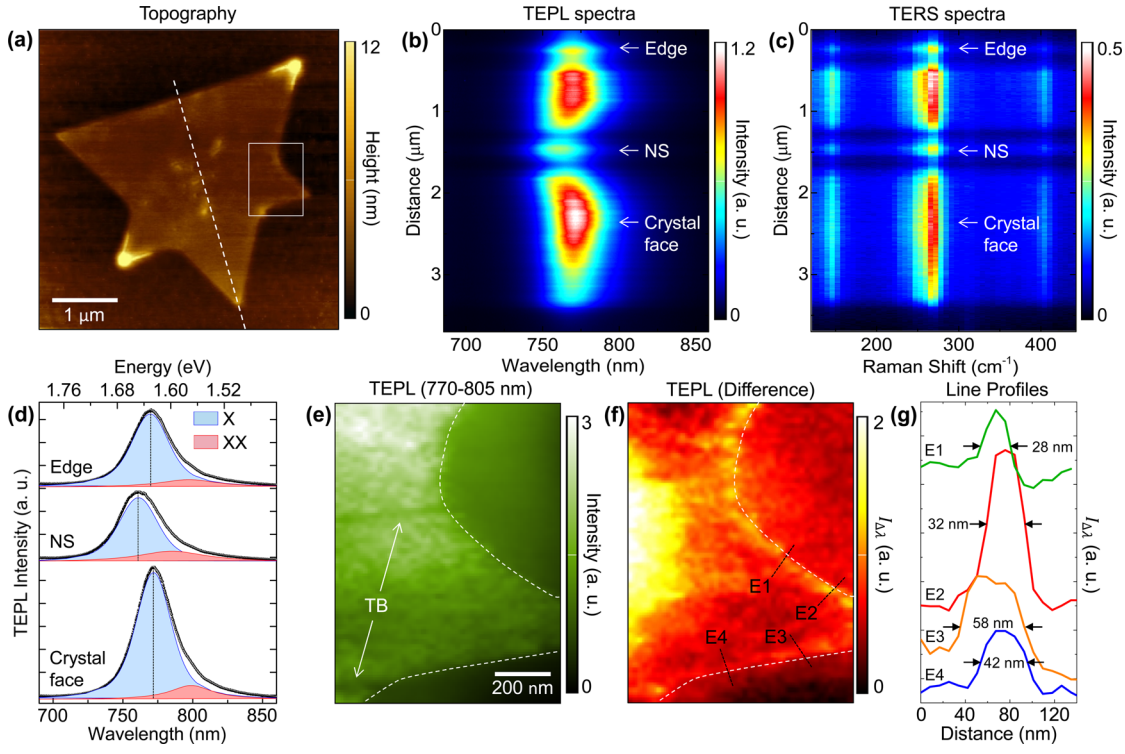

Figure 3. Topography (a) of a ML WSe_2 with spectral TEPL (b) and TERS (c) line traces along the center line of the crystal (dashed line in (a)). (d) Distinct TEPL spectra acquired from the edge, nucleation sites (NS), and grain face of crystal. Exciton and possible biexciton peaks are assigned via the Voigt fitting. Peak energies are 1.610 eV at edge, 1.630 eV at center, and 1.606 eV at crystal face. TEPL images of the spectral region of 770−805 nm (e) and the spectral difference (f). (g) Selected line profiles at the edge derived from (f).

dependent incident optics) exhibiting the expected optical antenna behavior with excitation polarization parallel with respect to the tip axis (experimental setup and observed spectra are shown in Figure S1b).

Figure 1c shows the distance dependence of TEPL and TERS of the ML WSe_2 with representative PL spectrum (black) acquired at 6 nm distance with Voigt profile fit dominated by the exciton response (∼1.61 eV) and a longer wavelength shoulder (∼1.55 eV). Figure 1d shows the near-field localization of both the TEPL and TERS responses for representative distances. The most prominent Raman peaks observed correspond to a superposition of E′ (in-plane) and A_1' (out-of-plane) modes at ∼273 cm^{-1},[24] and first- and third-order LA phonons (M point in the Brillouin zone) at ∼150 and ∼405

DOI: 10.1021/acs.nanolett.6b00238
Nano Lett. 2016, 16, 2621−2627

cm^{-1}, respectively.[25] The shoulder in the TEPL spectra (~10–3 nm distances) may rise from trion[21] or biexciton[11,26] emissions with the biexciton as the more likely origin for the following reasons: First, the ~50–60 meV spectral separation from the main exciton (X) peak is in agreement with the observation of biexciton assignment from previous studies.[11,26] Second, only a single exciton peak is observed in the far-field spectrum for the incident intensity of 10^5 W/cm^2 as shown in Figure 1d whereas the additional feature only emerges in the TEPL measurement with the tip-enhanced excitation intensity at the apex of ~10^7 W/cm^2. This behavior is consistent with the expected superlinear intensity dependence of biexciton emission (see Supporting Information for further discussion of biexciton emission).[27,28]

Following the initially continuous increase in both TEPL and TERS response for $d \lesssim 20$ nm, at distances $d < 5$ nm the WSe_2 PL starts to quench. This behavior is due to a near-field polarization transfer between the WSe_2 exciton and the metal tip, giving rise to nonradiative damping and PL quenching. The PL distance dependence observed is well described by a rate equation model with damping rates Γ and quantum yields of radiative emission η corresponding to $1/\Gamma_s \sim 0.5$ ps and $\eta_s \sim 0.1$ for the sample, and $1/\Gamma_{tip} \sim 30$ fs and $\eta_{tip} \sim 0.5$ for the tip, and with the resonance energy transfer length of $R_0 \sim 8$ nm. For TERS simulation, the same set of parameters are used except assuming very short ($1/\Gamma_s \sim 5$ fs) lifetime of the excitation to describe the instantaneous character of the Raman process (see Supporting Information for details).[29]

Results. *Multimodal TEPL/TERS Imaging of Nanoscale Defects.* We then image NS, external crystal edges, and TBs through their effect on the PL and Raman response. Figure 2a shows an ~500 nm spatial resolution confocal PL survey of a polycrystalline ML WSe_2 flake with spectrally integrated 770–805 nm acquisition. For the corresponding blueshifted PL image (725–760 nm) and difference PL image see Figure S3b,c. Corresponding TEPL images with ~15 nm spatial resolution reveal the influence of the NS region and crystal edge, which are seen to give rise to an associated decrease in PL intensity and spectral blueshift as shown in Figure 2d–f (770–805 nm region, 725–760 nm region, and calculated spectral difference image $I_{\Delta\lambda}$). Where $I_{\Delta\lambda} = \int_{\lambda_1}^{\lambda_2} |I(\lambda)_i - I(\lambda)_{ii}| d\lambda$, $\lambda_1 = 725$ nm, $\lambda_2 = 760$ nm, and $I(\lambda)_i$ and $I(\lambda)_{ii}$ are the PL spectra for blueshifted regions (NS and edges) and crystal faces, respectively.

Details of the effect of NS and crystal edges on the PL and Raman characteristics are investigated as shown in Figure 3, revealing in spatio-spectrally resolved line traces (panels b and c) the decrease in PL and blueshift, being more pronounced for the NS compared to the edges (Figure 3d). Intensity variations aside, no change in the corresponding Raman frequency of the E′ and A_1' superposition mode is observed (Figure 3c). The spatial variation of the PL at the edges (Figure 3e) is best exemplified in the spectral difference map (Figure 3f) with the PL shift and decrease extending irregularly along the edges, over an ~30–80 nm wide region, as also seen in representative line traces E1–E4 (Figure 3g).

The corresponding effect of the decrease in PL at the TBs can be clearly seen in the TEPL images Figures 2 and 3e and appears somewhat distinct from the effect of edges and NS, as further analyzed in Figure 4, showing a zoom in to a single TB (white box in Figure 2d). The TB is not discerned in the AFM topography (Figure 4a). Neither PL nor Raman emission

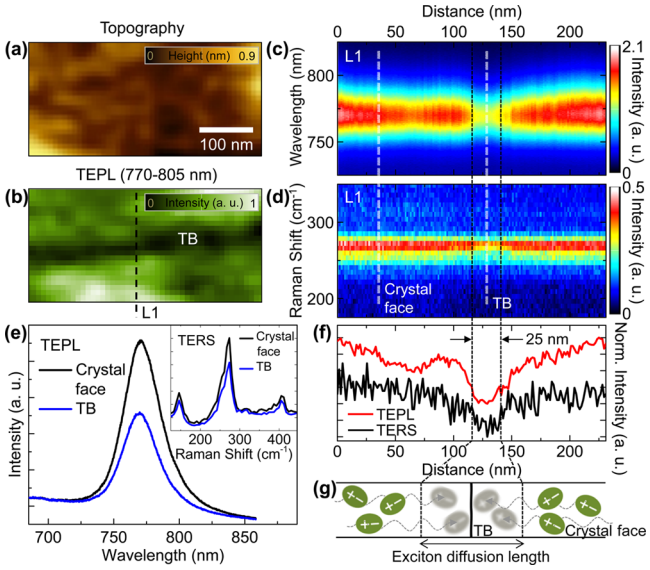

Figure 4. (a) AFM topography of TB area (indicated in Figure 2b). (b) TEPL image for the integrated intensity at 770–805 nm (indicated in Figure 2d). Spectral TEPL (c) and TERS (d) trace across TB (L1 indicated in (b)). (e) TEPL and TERS spectra derived from crystal face and TB regions indicated in (c) and (d) (dashed white lines). (f) Corresponding spectrally integrated line profiles for the 770 nm PL peak and 273 $^{-1}$ Raman mode derived from (c,d). (g) Illustration of exciton diffusion length at TB.

exhibit a spectral shift (Figure 4c–e); however, both experience a decrease comparable to the case of NS and edges. Yet the PL decrease is quite homogeneous along the twin boundary with a narrow width of ~25 nm (Figure 4f). Note that although we did not obtain correlated atomic resolution TEM or STM images of our specific samples, the symmetric mirror twinned boundary structures were confirmed by TEM studies for TMD crystal under similar conditions.[16]

Local Strain Engineering via Nanomechanical Force. In order to investigate the effect of local strain on the PL modification, we use the AFM tip to locally apply a contact force to perturb the sample while simultaneously measuring the TEPL. The bandgap of WSe_2 was shown to decrease linearly with increasing strain in the range of 0–2%.[30] Thus, we can use the energy of the PL peak to estimate the amount of strain for various tip–sample separations. From comparison with far-field PL of both as-grown and transferred WSe_2, we assess that the crystals are initially under a tensile strain of ~0.98%. (See Supporting Information and Figure S4 for details of strain estimation.)

Figure 5a shows that with increasing force exerted by the tip, the TEPL increases and spectral weight is transferred with the appearance of a blueshifted emission by ~48 meV. The nanomechanical tip interaction gives rise to an almost complete and irreversible strain release. In order to release the local strain and shift the bandgap by ~48 meV as shown in Figure 5a, the tip has to induce a stronger force onto the sample is therefore closer to the WSe_2 crystal compared to typical TEPL measurements. This leads to a significant quenching of the near-field PL such that the double peak curves in Figure 5a are dominated by the far-field response of the nearby strain released area. The near-field PL signal increases (blue curves) when the strain released area is expanded to ~200 × 200 nm^2. The PL modification at the strain released crystal region is seen in the confocal PL imaging before and after the force

DOI: 10.1021/acs.nanolett.6b00238
Nano Lett. 2016, 16, 2621–2627

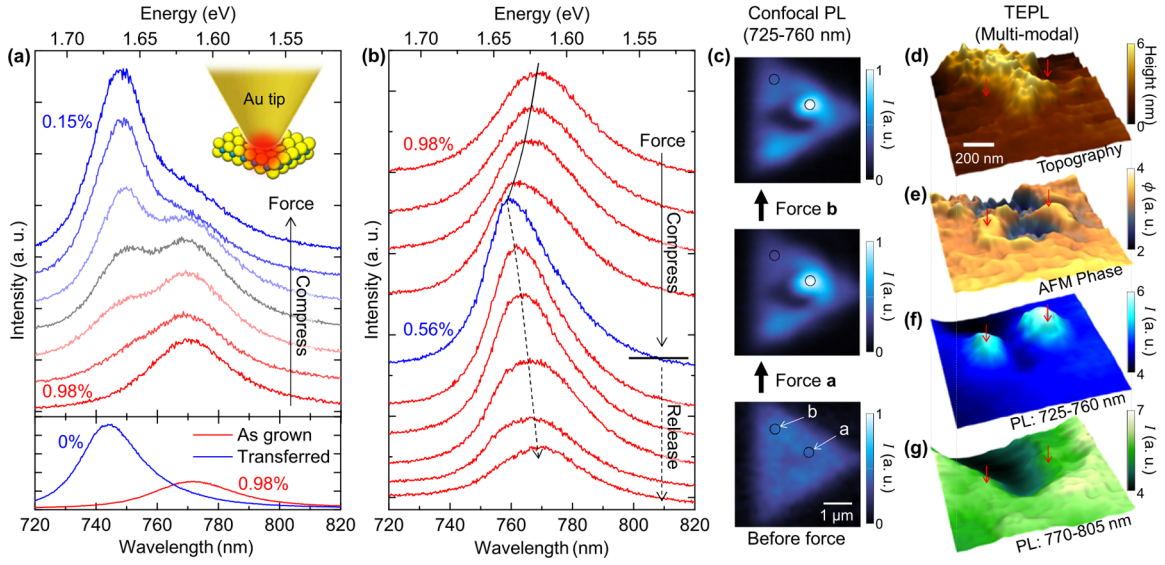

Figure 5. Evolution of TEPL spectra of the as-grown ML WSe_2 with increasing compressive force induced by the tip, giving rise to an irreversible release of the tensile strain of the crystal. Bottom: far-field reference PL spectra for the as-grown (red) and transferred (blue) ML WSe_2 on the SiO_2 substrates. (b) Reversible evolution of TEPL spectra under modest nanomechanical tip−sample force interaction. (c) Confocal PL (725−760 nm) images before and after irreversible (a) and reversible (b) strain manipulation. (d) AFM topography, (e) AFM phase, (f) blueshifted TEPL (725−760 nm), and (g) main TEPL (770−805 nm) images for two strain released locations near NS that exhibit low PL prior to nanomechanical strain release.

interaction (Figure 5c). Despite the only few tens of nanometers spatial localization of the apex force interaction, the strain released crystal region extends spatially over an ∼1 μm sized area. We estimate the maximum force exerted to ∼10 nN, without giving rise to tip apex modifications, as verified by repeated TEPL and TERS measurements. Figure 5d−g shows TEPL imaging on a WSe_2 flake near a NS region with initially strongly suppressed PL. Force interaction at the two locations indicated shows the appearance of blueshifted and enhanced PL. The associated strain release also manifests itself in a change in the AFM phase signal yet not in the topography as expected.

Under careful and weak force interaction, the strain can be partially released in a reversible fashion as shown in Figure 5b with a spectral shift of ∼24 meV corresponding to a maximum release to ∼0.56%. Both the reversible and irreversible strain release induced by the tip force interaction are generally repeatable with similar results for different flakes.

Discussion. Our results are generally consistent with the findings of recent studies that have addressed the localized modification of the PL by structural heterogeneities[16,17,21,22] yet add further spatial details and assignment to specific processes. An increase in PL intensity correlated with a spectral blueshift at GBs observed in ref 17 has been interpreted in terms of a local strain release and structural deformation, associated with the large TMD crystals studied (>10 μm) and the resulting high substrate strain accumulated in the growth process. Our correlated spectroscopic results and the ease of nanomechanical both reversible and irreversible local strain release by slight force perturbation would be consistent with this interpretation.

In contrast, recent near-field PL imaging revealed a decrease at GBs for small crystallites (<5 μm)[21] over an ∼120 nm average width and without spectral shifts. This, together with our finding of a PL quenching (47%) without changes in structure and bandgap at the TBs as concluded from the combined TERS and TEPL imaging, suggests that neither strain nor doping are responsible for the PL quenching but instead nonradiative recombination process possibly from midgap states of defects. Given the only atomic-scale dimensions of the TB, the spatial scale of PL quenching could be related to the exciton diffusion length. Our value for the PL quenching width of ∼25 nm would be in good agreement with the expected exciton diffusion length of ∼24 nm as estimated from the measured values of exciton diffusivity and lifetime.[16]

At the crystal edges, our observed decrease in PL intensity, spectral blueshift, and spatial heterogeneity agree with previous studies.[21] Similar to disordered semiconductors[31,32] the quenching could be due to energy funneling from higher to lower energy states in the inhomogeneous system.[21] Our spatial extent of the disordered PL modification region of ∼30−80 nm at the edges is in good agreement with the edge roughness observed by TEM.[16] Note that our length scale is significantly shorter than the ∼300 nm reported in a previous near-field PL study.[21] This difference in length scales could either be due to different crystal structures or growth conditions. Lastly, the significant PL quenching and blueshift at NS can be attributed to the loss of Se,[33] and surface adsorbates understood to be tungsten (W) compounds left in the growth process[34] that can act as nonradiative recombination sites.

The electronic band structure of TMDs is sensitive to tensile strain that causes reduced orbital hybridization due to the weakened ionic bonds.[35] This gives rise to a redshift of the bandgap energy and an associated decrease in PL intensity.[30,34,36,37] Our hybrid nanomechanical strain control and nanospectroscopy therefore not only confirms the role of strain in the optical and electronic heterogeneity of TMDs, but also allows to actively control the PL energy and quantum yield of nanoscale defects.

Conclusions. In summary, we have measured modifications of the electronic structure and optical properties of WSe_2 at the nanoscale through high resolution (<15 nm) multimodal TEPL and TERS imaging. A nonlocal PL modification at TBs associated with an ∼25 nm exciton diffusion length and a ∼30−

DOI: 10.1021/acs.nanolett.6b00238
Nano Lett. 2016, 16, 2621−2627

80 nm wide region of optical heterogeneity at edges is observed. Further, we have demonstrated dynamic tuning of the local bandgap of ML WSe_2 by releasing and controlling local strain. Our hybrid opto-mechanical nanoprobe technique can be used for tunable nanoelectronic devices where the carrier mobility is controlled via strain engineering.[34,36] We expect this method to help in the design of novel nano-photonic/electronic TMD devices by enabling local bandgap engineering and in situ spectroscopy of 2D materials.

Methods. *Sample Preparation.* WSe_2 monolayers were grown by physical vapor transport using powdered WSe_2 as precursor material. Source material (30 mg) in an alumina crucible was placed in the hot zone of a 25.4 mm horizontal tube furnace, and an SiO_2 substrate was placed downstream in a cooler zone at the edge of the furnace (750−850 °C). Before growth, the tube was evacuated to a base pressure of 0.13 mbar and purged several times with argon. The furnace was then heated to 970 °C at a rate of 35 °C/min and remained there for a duration of 5−10 min before cooling to room temperature naturally. A flow of 80 sccm argon and 20 sccm hydrogen was introduced as carrier gas during the 5−10 min growth period. Details can be found in ref 38.

TEPL/TERS Setup. Figure 1a shows a schematic of TEPL and TERS setup. The sample was mounted to a piezoelectric transducer (PZT, Attocube) for *xyz* scanning. Au tips were electrochemically etched with ∼10 nm apex radius[39] and attached to a quartz tuning fork (resonance frequency = ∼32 kHz). The electrically driven tuning fork was vibrated at its resonance frequency and the changing amplitude signal due to the shear-force was monitored for tip−sample distance control.[40] Tip positioning was operated by a stepper motor (MX25, Mechonics) and shear-force feedback and scanning conditions were controlled by a digital AFM controller (R9, RHK Technology). The incident laser beam was focused into the junction between the sample and the tip apex. The tip-enhanced PL and Raman signals were collected in back-scattered direction, passed through an edge filter (633 nm cutoff), and detected using a spectrometer (f = 500 mm, SpectraPro 500i, Princeton Instruments) with a $N_2(l)$ cooled charge-coupled device (CCD, Spec-10 LN/100BR, Princeton Instruments). The spectrometer was calibrated using hydrogen and mercury lines, and a 150 grooves/mm grating was used to obtain a high bandwidth spectrum for simultaneous measurement of TEPL and TERS.

Multimodal Imaging. The PL peak of ML WSe_2 at ∼1.61 eV (∼770 nm) and the PL intensity is uniform in the crystal face region whereas the PL intensity is decreased in the center and edge region and the peak position is blueshifted (see Figure S3a). The integrated intensities for the main PL (770−805 nm) and the blueshifted PL (725−760 nm) were selectively counted at each pixel of sample scanning. However, the spatial heterogeneity of the blueshifted PL was not clearly visualized because the tail of the main PL still significantly affects the integrated intensity of the blueshifted PL. To solve this problem, we subtracted the main PL image from the blueshifted PL image after compensating for the differences in intensity scale.

Therefore, the calculated subtracted image was directly proportional to the spectral region indicated in red (difference) in Figure 2(c). The spectral shifts were indeed small, and the large variations in overall intensity can mask these more subtle nanoscale variations at the sample features of interest. The selected spectral windows and image subtraction method were chosen to maximize contrast and enabled us to more clearly visualize these small effects at edges.

Local Strain Engineering. To control the local strain of as-grown WSe_2, the tip−sample distance was regulated by controlling the set-point and proportional-integral (PI) gains in feedback.[40] We set a low set-point and a high PI gain to apply mechanical force to the ML WSe_2. Through this force control of tip, the strain of the as-grown WSe_2 was locally released, as shown in Figure 5.

■ ASSOCIATED CONTENT

Supporting Information

Polarization dependence of tip plasmon, distance-dependent tip plasmon and photoluminescence, rate equation model for TEPL and TERS, multimodal imaging, bandgap energy as a function of strain, and PL quenching at grain boundaries. The Supporting Information is available free of charge on the ACS Publications website at DOI: 10.1021/acs.nanolett.6b00238.

(PDF)

■ AUTHOR INFORMATION

Corresponding Author

*E-mail: markus.raschke@colorado.edu.

Notes

The authors declare no competing financial interest.

■ ACKNOWLEDGMENTS

The authors would like to thank Ronald Ulbricht for many insightful discussions and advice with the experiments. Funding was provided by the U.S. Department of Energy, Office of Basic Sciences, Division of Material Sciences and Engineering, under Award No. DE-SC0008807.

■ REFERENCES

(1) Cui, X.; et al. *Nat. Nanotechnol.* **2015**, *10*, 534−540.
(2) Moody, G.; Kavir Dass, C. K.; Hao, K.; Chen, C.-H.; Li, L.-J.; Singh, A.; Tran, K.; Clark, G.; Xu, X.; Berghäuser, G.; Malic, E.; Knorr, A.; Li, X. *Nat. Commun.* **2015**, *6*, 8315.
(3) Qian, X.; Liu, J.; Fu, L.; Li, J. *Science* **2014**, *346*, 1344−1347.
(4) Kang, K.; Xie, S.; Huang, L.; Han, Y.; Huang, P. Y.; Mak, K. F.; Kim, C.-J.; Muller, D.; Park, J. *Nature* **2015**, *520*, 656−660.
(5) Koppens, F.; Mueller, T.; Avouris, P.; Ferrari, A.; Vitiello, M.; Polini, M. *Nat. Nanotechnol.* **2014**, *9*, 780−793.
(6) Mak, K. F.; Lee, C.; Hone, J.; Shan, J.; Heinz, T. F. *Phys. Rev. Lett.* **2010**, *105*, 136805.
(7) Splendiani, A.; Sun, L.; Zhang, Y.; Li, T.; Kim, J.; Chim, C.-Y.; Galli, G.; Wang, F. *Nano Lett.* **2010**, *10*, 1271−1275.
(8) Wang, Q. H.; Kalantar-Zadeh, K.; Kis, A.; Coleman, J. N.; Strano, M. S. *Nat. Nanotechnol.* **2012**, *7*, 699−712.
(9) Mak, K. F.; He, K.; Shan, J.; Heinz, T. F. *Nat. Nanotechnol.* **2012**, *7*, 494−498.
(10) Kuc, A.; Zibouche, N.; Heine, T. *Phys. Rev. B: Condens. Matter Mater. Phys.* **2011**, *83*, 245213.
(11) Jones, A. M.; Yu, H.; Ghimire, N. J.; Wu, S.; Aivazian, G.; Ross, J. S.; Zhao, B.; Yan, J.; Mandrus, D. G.; Xiao, D.; Yao, W.; Xu, X. *Nat. Nanotechnol.* **2013**, *8*, 634−638.
(12) Xu, X.; Yao, W.; Xiao, D.; Heinz, T. F. *Nat. Phys.* **2014**, *10*, 343−350.
(13) Yin, X.; Ye, Z.; Chenet, D. A.; Ye, Y.; O'Brien, K.; Hone, J. C.; Zhang, X. *Science* **2014**, *344*, 488−490.
(14) Cheng, J.; Jiang, T.; Ji, Q.; Zhang, Y.; Li, Z.; Shan, Y.; Zhang, Y.; Gong, X.; Liu, W.; Wu, S. *Adv. Mater.* **2015**, *27*, 4069−4074.
(15) Chow, P. K.; Jacobs-Gedrim, R. B.; Gao, J.; Lu, T.-M.; Yu, B.; Terrones, H.; Koratkar, N. *ACS Nano* **2015**, *9*, 1520−1527.

DOI: 10.1021/acs.nanolett.6b00238
Nano Lett. 2016, 16, 2621−2627

(16) van der Zande, A. M.; Huang, P. Y.; Chenet, D. A.; Berkelbach, T. C.; You, Y.; Lee, G.-H.; Heinz, T. F.; Reichman, D. R.; Muller, D. A.; Hone, J. C. *Nat. Mater.* **2013**, *12*, 554−561.
(17) Liu, Z.; et al. *Nat. Commun.* **2014**, *5*, 5246.
(18) Najmaei, S.; Liu, Z.; Zhou, W.; Zou, X.; Shi, G.; Lei, S.; Yakobson, B. I.; Idrobo, J.-C.; Ajayan, P. M.; Lou, J. *Nat. Mater.* **2013**, *12*, 754−759.
(19) Huang, Y. L.; Chen, Y.; Zhang, W.; Quek, S. Y.; Chen, C.-H.; Li, L.-J.; Hsu, W.-T.; Chang, W.-H.; Zheng, Y. J.; Chen, W.; Wee, A. T. S. *Nat. Commun.* **2015**, *6*, 6298.
(20) Park, S.; Kim, M. S.; Kim, H.; Lee, J.; Han, G. H.; Jung, J.; Kim, J. *ACS Nano* **2015**, *9*, 11042−11048.
(21) Bao, W.; et al. *Nat. Commun.* **2015**, *6*, 7993.
(22) Lee, Y.; Park, S.; Kim, H.; Han, G. H.; Lee, Y. H.; Kim, J. *Nanoscale* **2015**, *7*, 11909−11914.
(23) Neacsu, C. C.; Steudle, G. A.; Raschke, M. B. *Appl. Phys. B: Lasers Opt.* **2005**, *80*, 295−300.
(24) Chen, S.-Y.; Zheng, C.; Fuhrer, M. S.; Yan, J. *Nano Lett.* **2015**, *15*, 2526−2532.
(25) Zhao, W.; Ghorannevis, Z.; Amara, K. K.; Pang, J. R.; Toh, M.; Zhang, X.; Kloc, C.; Tan, P. H.; Eda, G. *Nanoscale* **2013**, *5*, 9677−9683.
(26) You, Y.; Zhang, X.-X.; Berkelbach, T. C.; Hybertsen, M. S.; Reichman, D. R.; Heinz, T. F. *Nat. Phys.* **2015**, *11*, 477−481.
(27) Shang, J.; Shen, X.; Cong, C.; Peimyoo, N.; Cao, B.; Eginligil, M.; Yu, T. *ACS Nano* **2015**, *9*, 647−655.
(28) Kim, M. S.; Yun, S. J.; Lee, Y.; Seo, C.; Han, G. H.; Kim, K. K.; Lee, Y. H.; Kim, J. *ACS Nano* **2016**, *10*, 2399−2405.
(29) Kravtsov, V.; Berweger, S.; Atkin, J. M.; Raschke, M. B. *Nano Lett.* **2014**, *14*, 5270−5275.
(30) Desai, S. B.; Seol, G.; Kang, J. S.; Fang, H.; Battaglia, C.; Kapadia, R.; Ager, J. W.; Guo, J.; Javey, A. *Nano Lett.* **2014**, *14*, 4592−4597.
(31) Laquai, F.; Park, Y.-S.; Kim, J.-J.; Basché, T. *Macromol. Rapid Commun.* **2009**, *30*, 1203−1231.
(32) Kagan, C.; Murray, C.; Nirmal, M.; Bawendi, M. *Phys. Rev. Lett.* **1996**, *76*, 1517.
(33) Liu, B.; Fathi, M.; Chen, L.; Abbas, A.; Ma, Y.; Zhou, C. *ACS Nano* **2015**, *9*, 6119−6127.
(34) Cong, C.; Shang, J.; Wu, X.; Cao, B.; Peimyoo, N.; Qiu, C.; Sun, L.; Yu, T. *Adv. Opt. Mater.* **2014**, *2*, 131−136.
(35) He, K.; Poole, C.; Mak, K. F.; Shan, J. *Nano Lett.* **2013**, *13*, 2931−2936.
(36) Conley, H. J.; Wang, B.; Ziegler, J. I.; Haglund, R. F., Jr; Pantelides, S. T.; Bolotin, K. I. *Nano Lett.* **2013**, *13*, 3626−3630.
(37) Castellanos-Gomez, A.; Roldán, R.; Cappelluti, E.; Buscema, M.; Guinea, F.; van der Zant, H. S.; Steele, G. A. *Nano Lett.* **2013**, *13*, 5361−5366.
(38) Clark, G.; Wu, S.; Rivera, P.; Finney, J.; Nguyen, P.; Cobden, D. H.; Xu, X. *APL Mater.* **2014**, *2*, 101101.
(39) Neacsu, C. C.; Dreyer, J.; Behr, N.; Raschke, M. B. *Phys. Rev. B: Condens. Matter Mater. Phys.* **2006**, *73*, 193406.
(40) Karrai, K.; Grober, R. D. *Appl. Phys. Lett.* **1995**, *66*, 1842−1844.

DOI: 10.1021/acs.nanolett.6b00238
Nano Lett. 2016, 16, 2621−2627